IEEE Robotics and Automation Letters (RA-L) paper, presented at ICRA 2026, Vienna, Austria. Cite as RA-L paper.

# Deep Learning–Driven Tumor Boundary Estimation using Robotic Palpation in Minimally Invasive Surgery

Youngjun Ryu, Jeongbin Hong, Hyeonwoo Kee, Joowon Park, and Sukho Park*, *Member, IEEE*

***Abstract*— Accurate estimation of tumor boundaries is critical for ensuring adequate surgical margins in robot-assisted minimally invasive surgery (RMIS). In this study, we present a method that estimates tumor boundaries in RMIS using sweeping palpation data acquired with a single force/torque (F/T) sensor. From the reconstructed surface, tissue displacement and normal force were derived to calculate stiffness, which was then used to construct a stiffness map. To reduce noise and enhance feature representations, we employed a sparse autoencoder (SAE). The SAE outputs were subsequently clustered with a Gaussian mixture model (GMM) and K-means to segment the tumor from normal tissue. Experiments with phantom models and an *ex vivo* model demonstrated that the SAE-based approach significantly improved the Dice similarity coefficient (DSC) and sensitivity while maintaining specificity, and reduced the Hausdorff distances (HD and HD95) and average symmetric surface distance (ASSD), compared with results from raw data. Importantly, when evaluated under clinically relevant surgical margin conditions, the estimated HD consistently remained below threshold across all models. These results indicate that the proposed method achieves both high accuracy and clinical feasibility without additional imaging devices or displacement sensors, highlighting its potential to support margin minimization and organ function preservation in RMIS.**

***Index Terms*— Deep learning, Palpation, Robot-assisted minimally invasive surgery, Stiffness estimation, Tumor boundary detection**

## I. Introduction

Modern surgical practice has increasingly focused on precision and minimally invasive approaches, with the goals of shortening patient recovery time and minimizing postoperative complications. Robot-assisted minimally invasive surgery (RMIS) has emerged as a promising technology that improves surgical precision, reduces dependence on surgeon-specific manual skills, and holds significant potential to improve patient outcomes [1], [2]. RMIS utilizes robotic arms equipped with fine manipulation capabilities, in conjunction with specialized surgical instruments, to facilitate more precise identification and resection of lesions through smaller incisions compared to traditional open or laparoscopic surgery. Such approaches shorten recovery time and reduce blood loss and postoperative complication rates [3], [4]. RMIS has been applied to precision resections of various soft tissue organs, such as the kidney and liver. In procedures where organ function preservation is critical, such as partial nephrectomy or parenchyma-sparing liver resection, the ability to accurately and continuously detect tumor boundaries in real time is particularly important [5], [6].

Tumor boundary detection is essential for ensuring adequate surgical margins and achieving complete resection. It is directly linked to the risk of residual cancer cells, thereby playing a critical role in preventing local recurrence and improving long-term survival [7]. A surgical margin refers to the boundary that encompasses the tumor together with adjacent normal tissue. If the margin is excessively wide, it can cause unnecessary tissue loss and compromise organ function [8]. Therefore, precise estimation of tumor boundaries is essential to balance oncologic safety with functional preservation.

Conventional RMIS approaches have relied on medical imaging modalities such as CT, MRI, and ultrasound to analyze tumor morphology and delineate boundaries [9], [10], [11]. However, these image-based methods depend on static preoperative data and therefore cannot account for tissue deformation or displacement that occurs intraoperatively from patient repositioning, respiratory motion, or instrument interaction [12], [13]. As a result, discrepancies may arise between preoperative images and intraoperative anatomy, potentially undermining surgical precision and safety [14].

Robotic palpation has been proposed as an effective alternative to overcome these limitations. In this approach, force and displacement data are collected as the robotic end-effector interacts with tissue, and tissue stiffness is quantitatively estimated based on these measurements [15], [16]. Previous studies have reported that tumor tissue exhibits approximately two- to tenfold greater stiffness than normal tissue [17]. Accordingly, force–displacement analysis provides a means of indirectly inferring tumor presence and localization

Received 11 September 2025; accepted 18 December 2025. Date of publication 12 January 2026; date of current version 2 February 2026. This article was recommended for publication by Associate Editor L. Cao and Editor J. Burgner-Kahrs upon evaluation of the reviewers' comments. This work was supported in part by Basic Science Research Program through the National Research Foundation of Korea (NRF), in part by the Ministry of Education under Grant RS-2025-25420118, in part by the Industrial Strategic Technology Development Program, and in part by the Ministry of Trade, Industry & Energy (MOTIE, Korea) under Grant 20017903. (Corresponding author: Sukho Park.) Youngjun Ryu, Jeongbin Hong, Hyeonwoo Kee, and Sukho Park are with the MMR Laboratory, Daegu Gyeongbuk Institute of Science and Tech-nology, Daegu 42988, Republic of Korea (e-mail: ryu0snail@dgist.ac.kr; bsb05028@dgist.ac.kr; mequee@dgist.ac.kr; shpark12@dgist.ac.kr).

Joowon Park is with the University of Ulsan, Ulsan 44610, Republic of Korea (e-mail: jwpark12@ulsan.ac.kr).

This article has supplementary downloadable material available at https://doi.org/10.1109/LRA.2026.3653373, provided by the authors.

Digital Object Identifier 10.1109/LRA.2026.3653373

[18]. In RMIS settings, however, precise estimation of tissue properties is particularly challenging due to limited visualization, confined workspace, and restricted instrument maneuverability [19]. For this reason, most previous studies have employed indentation-based robotic palpation techniques [20], [21], [22], [23], [24]. This method offers the advantage of relatively easy acquisition of force data through force/torque (F/T) or pressure sensors. However, accurate displacement measurement requires additional equipment, such as endoscopic cameras, or depth cameras [25], [26]. These vision-based approaches can estimate surface deformation or geometry, but they remain limited to optical visibility and cannot directly capture subsurface mechanical contrasts that are critical for tumor detection [27]. While emerging soft tactile technologies like polymer-based skins and fiber-optic arrays show promise, their application in RMIS is limited by fabrication complexity, hysteresis, signal drift, and calibration instability [28], [29].

To address these limitations, a sweeping palpation strategy has been proposed. In this approach, the robotic end-effector continuously collects force data while sweeping the organ surface, enabling efficient characterization of the mechanical properties over a wide area [30], [31]. However, because displacement is difficult to measure during sweeping palpation, conventional stiffness estimation techniques designed for indentation cannot be directly applied. Consequently, the generation of high-resolution stiffness maps within the region of interest (ROI) is restricted, limiting the accuracy of tumor boundary estimation [32], [33]. Therefore, achieving precise stiffness estimation using only a single F/T sensor—without auxiliary sensing devices—and leveraging these measurements to analyze the mechanical properties of the tissue over a wide area is a clinically important challenge. Furthermore, incorporating deep learning methods into stiffness data processing can enhance the contrast between tissue types and improve boundary estimation accuracy [34], [35]. The combined use of sweeping palpation and deep learning holds substantial promise for improving both the accuracy and real-time performance of stiffness-based tumor boundary detection. In this study, we propose a novel method for accurate tumor boundary estimation over the entire ROI by combining stiffness mapping with unsupervised clustering. Specifically, we integrate force and displacement data by utilizing reconstructed surface point cloud information together with robotic kinematics, thereby enabling the generation of precise stiffness maps without requiring additional sensors. The resulting stiffness data are then processed through an autoencoder based on a multilayer perceptron (MLP) to extract latent features, after which clustering is performed on the reconstructed output to quantitatively estimate tumor boundaries.

The key contributions of this work are summarized as follows:

(1) We propose a novel two-step robotic palpation workflow that reconstructs the 3D tissue surface and utilizes this geometric prior to enable accurate stiffness estimation during sweeping palpation thus overcoming the fundamental displacement-measurement limitations of conventional sweeping methods.

(2) We demonstrate a high-resolution stiffness mapping framework using only a single F/T sensor, eliminating the need for auxiliary displacement or vision-based sensors and significantly simplifying the sensing pipeline for RMIS.

(3) We show that MLP-based autoencoder latent features substantially improve clustering robustness, thereby enhancing tumor boundary estimation accuracy compared to direct stiffness-based classification.

## II. Method

### A. Overall Process

The proposed tumor boundary detection process in this study comprises three main steps: (1) surface reconstruction, (2) stiffness estimation, and (3) tumor boundary estimation. The overall workflow is schematically depicted in Fig. 1.

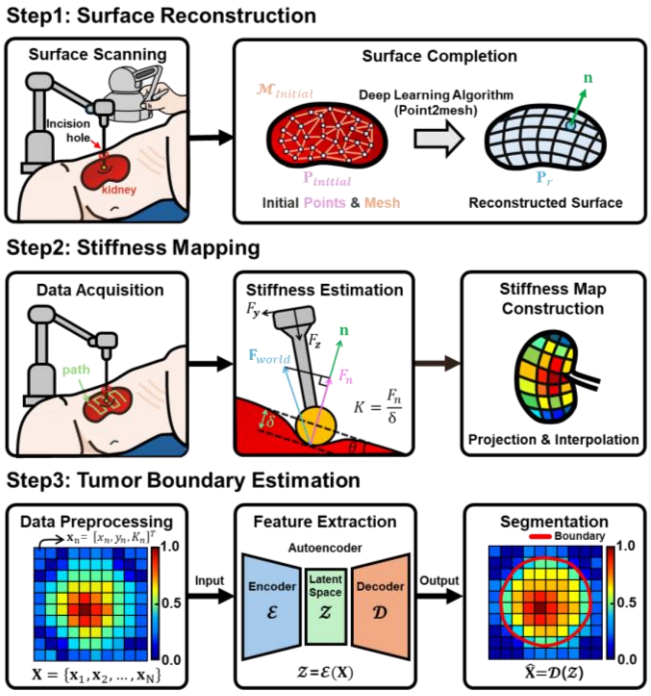


**Fig. 1.** Overall schematic process. Step 1: Surface reconstruction, Step 2: Stiffness mapping, and Step 3: Tumor boundary estimation.

#### *Step 1: Surface Reconstruction*

First, the raw surface data of the soft tissue ($\mathbf{P}_{Initial}$) was collected via teleoperation by tracking the position of the robotic end-effector. Based on the initial mesh ($\boldsymbol{\mathcal{M}}_{Initial}$) generated through a ball-pivoting algorithm applied to the collected points, the Point2Mesh deep learning algorithm was employed to reconstruct the incomplete surface and fill in missing regions. From this reconstruction, a fully reconstructed surface point cloud ($\mathbf{P}_r$) along with its corresponding normal vector ($\mathbf{n}$) was obtained.

#### *Step 2: Stiffness Mapping*

Next, a palpation path is planned along the reconstructed organ surface to guide the robot end-effector. The end-effector then executes sweeping palpation along this path, during which force, position, and joint angle data are continuously recorded. Using forward kinematics, the robot's pose is

determined, and the normal contact force is calculated. The displacement (δ) at each contact point is estimated by measuring the positional difference between the end-effector and the reconstructed surface point cloud using a *k*-nearest neighbor (*k*-NN) search algorithm. Finally, stiffness values are computed by integrating force and displacement data, and a spatially uniform stiffness map is produced through interpolation.

*Step 3: Tumor Boundary Estimation*

In the final step, the stiffness map serves as the basis for unsupervised estimation of the tumor boundary. Each surface point is represented as a three-dimensional feature vector comprising its spatial position $(x, y)$ and stiffness value $(K)$. These feature vectors are input into a sparse autoencoder implemented with a multilayer perceptron (MLP), where they are compressed into a low-dimensional latent representation and subsequently reconstructed. To segment tumor and normal regions quantitatively, Gaussian mixture models (GMM) and K-means clustering are applied to the reconstructed stiffness map. The accuracy of boundary estimation is then assessed using region-based metrics (Dice similarity coefficient (DSC), sensitivity, and specificity) and distance-based metrics (Hausdorff distance [HD and HD95] and average symmetric surface distance [ASSD]).

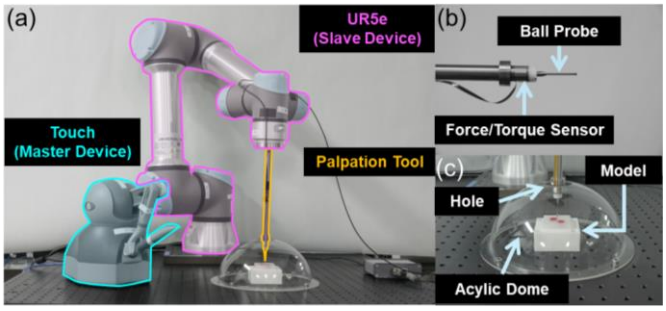


**Fig. 2.** Experimental setup. (a) Robotic palpation system, (b) Palpation probe and sensor, and (c) Experiment setup under RMIS environment.

## B. Experimental Setup

In this study, robotic palpation was performed in a simulated RMIS environment to collect stiffness data. As shown in Fig. 2, the overall experimental setup consists of (i) a master–slave teleoperation system, (ii) a palpation tool equipped with a F/T sensor and a ball probe, and (iii) an RMIS-simulated experimental environment.

Fig. 2(a) presents the complete robotic palpation system. The master device is a Touch haptic interface (3D Systems Inc.), while the slave device is a UR5e robotic arm (Universal Robots A/S). The system is operated on Ubuntu 18.04.01 LTS with a Xenomai 3.2 kernel, running at a 2 ms control loop to enable real-time teleoperation. Fig. 2(b) illustrates the palpation tool mounted on the UR5e end-effector. A 6-axis Hex12 F/T sensor (Resense GmbH) records interaction forces and torques, and a 2 mm-diameter ball probe is affixed to the distal end. This design enables continuous and wide-area sweeping palpation while reducing the risk of soft tissue damage. Fig. 2(c) depicts the experimental environment, in which an acrylic dome structure replicates RMIS conditions. The palpation tool is inserted through a port at the dome apex, with a remote center of motion (RCM) constraint applied to reproduce the kinematic constraints of laparoscopic surgery.

Specifically, the tissue-mimicking phantom models were fabricated by mixing Ecoflex 00-30 (Smooth-On Inc.) with silicone thinner (Smooth-On Inc.), using different mixing ratios to distinguish between normal and tumor tissues. Tumor phantoms (colored red) were prepared by mixing Ecoflex 00-30A and 00-30B in a 1:1 ratio, whereas normal phantoms (colored white) were created by mixing Ecoflex 00-30A, 00-30B, and silicone thinner in a 1:1:1 ratio. For the *ex vivo* model, artificial tumors were formed by blending agarose gel, contrast medium, and deionized (DI) water in a 1:3:22 ratio, and subsequently implanted into porcine kidneys. For the phantom models, ground-truth masks were generated by delineating the outer boundaries according to the design geometry, while for the *ex vivo* model, ground-truth masks were derived by localizing the location of the implanted tumors from post-experimental CT images.

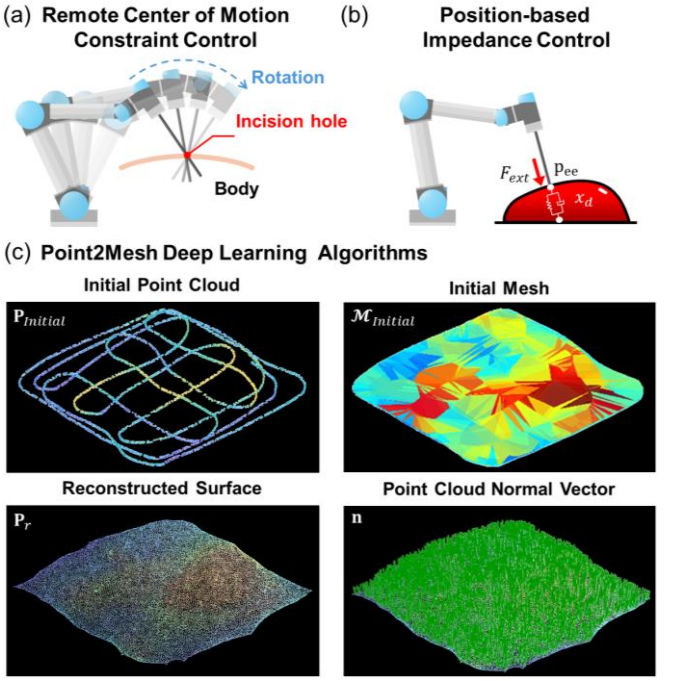


**Fig. 3.** Surface reconstruction process. (a) Remote center of motion (RCM) constraint control, (b) Position-based impedance control, and (c) Point2Mesh deep learning algorithm.

## C. Surface Reconstruction

In this study, we aimed to develop a technique for minimally invasive surgery (MIS) that does not rely on image-based information, instead utilizing point cloud data of soft tissue to reconstruct the surface of the region of interest (ROI) [36]. The surface reconstruction stage functions as a preprocessing procedure for generating palpation paths on the soft tissue surface and for estimating displacement data. As illustrated in Fig. 1(a), the surface reconstruction process is divided into two major procedures.

The first procedure involves surface scanning through teleoperation. When the operator manipulates the master device, the slave robot synchronously replicates the motion,

and the positions of the end-effector in contact with the target surface are recorded to form the initial point cloud. As shown in Fig. 3(a) and (b), both RCM constraint control and position-based impedance control are applied to the slave robot to ensure safe operation. The RCM constraint enforces the geometric requirement that surgical instruments in MIS pivot about the incision point. By controlling the slave robot relative to a virtual incision hole, this constraint preserves a minimal incision. To realize the desired trajectory under this constraint, the controller solves a Jacobian-based constrained inverse kinematics formulation to compute the joint motions necessary to achieve the target end-effector pose [37].

In addition, position-based impedance control ensures that the slave's actual position $x$ relative to the commanded target position $x_d$ follows the dynamics of a virtual mass–damper–spring system, thereby improving safety and compliance during teleoperation [38].

$$M\ddot{\tilde{x}} + B\dot{\tilde{x}} + K\tilde{x} - F_{ext} = u \tag{1}$$

where $\tilde{x}$ denotes the position error, $M$ the virtual mass, $B$ the virtual damper, $K$ the virtual spring, $F_{ext}$ the external force, and $u$ the control input.

The second procedure is surface completion. Since the teleoperated data acquisition may not fully capture the entire ROI, a Point2Mesh-based deep learning algorithm was applied to recover the missing regions [39]. Point2Mesh is a convolutional neural network-based unsupervised learning method that takes as input the initial point cloud and the mesh generated via the ball-pivoting algorithm, and reconstructs a high-fidelity surface [40]. As shown in Fig. 3(c), this process produces the final reconstructed surface point cloud ($\mathbf{P}_r$) along with the corresponding surface normal vector ($\mathbf{n}$).

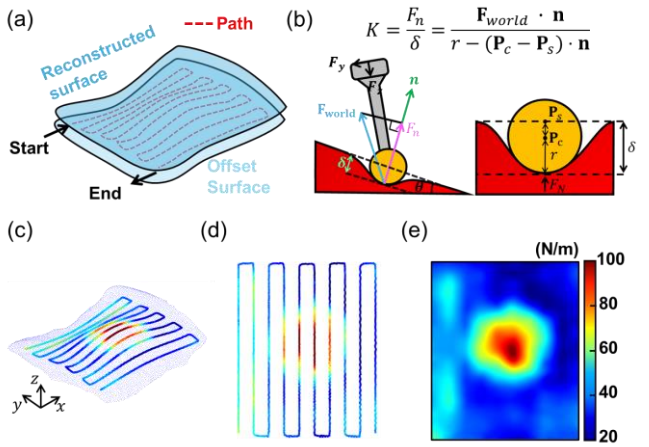


**Fig. 4.** Stiffness mapping process. (a) Path generation using regression line on offset surface, (b) Stiffness estimation method, (c) Stiffness data acquisition along sweeping palpation path, (d) Orthogonal projection of stiffness values onto the XY plane, and (e) Final interpolated stiffness map.

### *D. Stiffness Mapping*

The stiffness mapping step comprises three procedures: generating exploration paths from the reconstructed surface, acquiring stiffness data via sweeping palpation, and constructing the final stiffness map.

The first procedure is data acquisition, during which force data are recorded through sweeping palpation. As illustrated in Fig. 4(a), an offset surface with a predefined displacement is generated toward the lesion, based on the reconstructed surface. Multiple regression lines are then applied using least-squares regression to plan the palpation paths for the robotic palpation system [41]. While the end-effector follows these designed paths, force data are collected via the F/T sensor mounted on the palpation tool, and the probe center coordinates $\mathbf{P}_c$ are computed using forward kinematics.

The second procedure, stiffness estimation, is shown in Fig. 4(b). In this procedure, stiffness is estimated using the force-position data obtained during the data acquisition stage together with the reconstructed surface point cloud. The force measured by the F/T sensor,

$$\mathbf{F}_{sensor} = \left[F_x, F_y, F_z\right]^T \tag{2}$$

is expressed in the sensor frame and then transformed into the world frame force $\mathbf{F}_{world}$ using the following relation:

$$\mathbf{F}_{world} = \mathbf{R}_{sensor}^{world} \cdot \mathbf{F}_{sensor} \tag{3}$$

where $\mathbf{R}_{sensor}^{world}$ is the rotation matrix from the sensor frame to the world frame, obtained through forward kinematics. The unit normal vector $\mathbf{n}$ is extracted from the reconstructed surface model, and the normal force magnitude is computed as:

$$F_n = \mathbf{F}_{world} \cdot \mathbf{n} \tag{4}$$

The palpation displacement is calculated using the probe center position $\mathbf{P}_c$ and the contact point on the surface $\mathbf{P}_s$, and the probe radius $r$. Specifically, $\mathbf{P}_s$ is approximated as the contact point by selecting the nearest neighbors of $\mathbf{P}_c$ from the reconstructed surface point cloud $\mathbf{P}_r$ through the $k$-NN search (Euclidean distance, with $k = 10$), and averaging their positions [42]. The displacement is then defined as:

$$\delta = \begin{cases} r - (\mathbf{P}_c - \mathbf{P}_s) \cdot \mathbf{n}, & \text{if } (\mathbf{P}_c - \mathbf{P}_s) \cdot \mathbf{n} < r \\ 0, & \text{otherwise} \end{cases} \tag{5}$$

Finally, the stiffness K is calculated as follows:

$$K = \frac{F_n}{\delta} = \frac{\mathbf{F}_{world} \cdot \mathbf{n}}{r - (\mathbf{P}_c - \mathbf{P}_s) \cdot \mathbf{n}} \tag{6}$$

The third procedure, stiffness map construction, is depicted in Fig. 4(c)–(e). In this procedure, the stiffness values calculated at each point are spatially interpolated to generate the final 2D stiffness map. Fig. 4(c) illustrates the raw stiffness measurements obtained along the sweeping palpation paths, while Fig. 4(d) presents their orthogonal projection onto the XY-plane. Finally, Fig. 4(e) displays the completed stiffness map, created by interpolating the scattered data with MATLAB *scatteredInterpolant* function, subsequently applying Gaussian smoothing ($\sigma = 3$).

### E. Tumor Boundary Estimation

As shown in Fig. 1(c), the tumor boundary estimation process is composed of three procedures: data preprocessing, mechanical feature extraction, and segmentation via clustering. In this process, the stiffness map generated in the previous section is utilized to extract tumor-related features, and unsupervised feature learning combined with clustering

algorithms is employed to detect tumor boundaries. In the first process, data preprocessing, each sample is extracted from the stiffness map and represented as an input vector defined by

$$\mathbf{x}_n = [x_n, y_n, K_n]^T \in \mathbb{R}^3 \quad (7)$$

where $(x_n, y_n)$ denote the spatial coordinates, while $K_n$ represents the normalized stiffness value. The dataset consists of a total of $N = 40{,}000$ samples.

Second, the mechanical feature extraction, illustrated in Fig. 5(a), extracts features from the 2D stiffness map using a sparse autoencoder (SAE). The left panel shows the stiffness map obtained in the previous section, the center depicts the encoder–decoder architecture, and the right panel presents the reconstructed output produced by SAE. This process reduces noise in the original data while enhancing tumor-related features. Through SAE, dimensionality reduction and feature learning are achieved by minimizing a composite loss function that combines reconstruction loss, weight regularization, and sparsity constraints, defined as follows [43].

$$\mathcal{L} = \frac{1}{N}\sum_{n=1}^{N}\|\mathbf{x}_n - \hat{\mathbf{x}}_n\|^2 + \lambda\sum_{l}\left\|\mathbf{W}^{(l)}\right\|_F^2 + \beta\sum_{j=1}^{Z} KL(\rho \parallel \hat{\rho}_j) \quad (8)$$

where $\hat{\mathbf{x}}_n$ denotes the reconstruction output, $\mathbf{W}^{(l)}$ represents the weight matrix of the $l$-th layer, $\lambda$ is the regularization coefficient, $\beta$ is the sparsity penalty coefficient, $Z$ is the number of hidden units, $\rho$ is the target sparsity ratio and $\hat{\rho}_j$ is the average activation of the $j$-th hidden unit. The Kullback–Leibler (KL) divergence is defined as follows [44].

$$KL(\rho \parallel \hat{\rho}_j) = \rho\log\frac{\rho}{\hat{\rho}_j} + (1-\rho)\log\frac{1-\rho}{1-\hat{\rho}_j} \quad (9)$$

Finally, the SAE-reconstructed outputs were segmented using two clustering methods, GMM and K-means, as shown in Fig. 5(b). These clustering approaches are well-suited for tumor boundary detection because they can automatically distinguish between tumor and normal tissue based on the intrinsic structure of the stiffness distribution, without the need for prior labeling. The clustering algorithms function by optimizing their respective objective functions [45], [46].

*(1) GMM Objective function*

$$J_{GMM} = \underset{\Theta}{\operatorname{argmax}}\sum_{n=1}^{N}\log\left(\sum_{j=1}^{C}\pi_j\mathcal{N}(\hat{\mathbf{x}}_n|\mu_j,\Sigma_j)\right) \quad (10)$$

Here, $C$ is the number of clusters, $\pi_j$ denotes the mixing coefficient, $\mu_j$ the mean vector, $\Sigma_j$the covariance matrix, and $\Theta = \{\pi_j, \mu_j, \Sigma_j\}_{j=1}^{C}$ represents the complete set of parameters.

*(2) K-means Objective function*

$$J_{K-means} = \min_{\boldsymbol{S}}\sum_{j=1}^{C}\sum_{\hat{x}_n \epsilon S_j}\left\|\hat{\mathbf{x}}_n - \mu_j\right\|^2 \quad (11)$$

Here, $S_j$ denotes the subset of samples assigned to the j-th cluster, and $\boldsymbol{S} = \{S_1, S_2, \ldots, S_C\}$ represents the overall clustering result of the dataset.

Fig. 5(c) compares the tumor boundary estimation results. The left panel illustrates the original stiffness map prior to SAE processing, whereas the right panel presents the reconstructed output generated by SAE. This comparison demonstrates that SAE-based feature representations provide clearer tumor boundary delineation and greater clustering stability. Model training was performed using the trainAutoencoder function in MATLAB Deep Learning Toolbox, with optimization conducted via the scaled conjugate gradient (SCG) algorithm. The number of training epochs was set to 300, with parameters $\lambda = 0.02$, $C = 2$, $\beta = 15$, and $\rho = 0.016$. All training was executed on a workstation equipped with an Intel i7-12700 CPU (2.10 GHz), 32 GB RAM, and an NVIDIA RTX 3060 GPU. To ensure robustness against randomness in initialization, each clustering experiment was repeated 30 times, and the resulting quantitative metrics are reported as mean ± standard deviation.

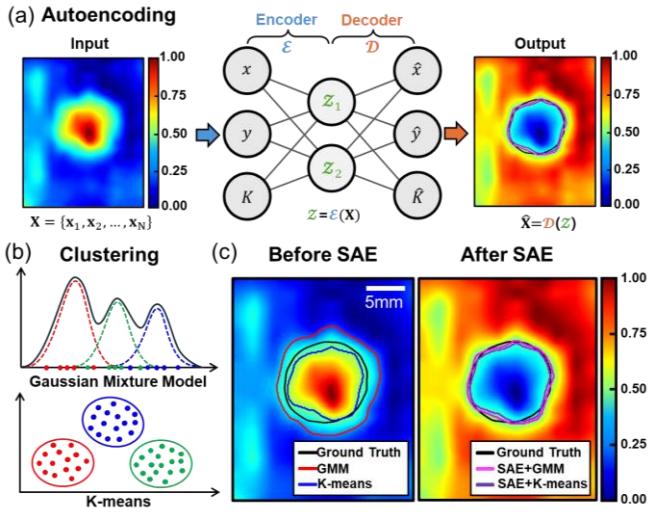


**Fig. 5.** Tumor boundary estimation process. (a) Extraction of discriminative feature from the original stiffness map using a sparse autoencoder (SAE), (b) Application of clustering models (GMM and K-means) to the extracted stiffness features, and (c) Comparison of tumor boundary estimations before (left) and after (right) applying SAE.

## III. Experimental Results

### *A. Tumor boundary estimation*

In this study, the proposed SAE-based feature extraction and clustering method was applied to multiple phantom models and an *ex vivo* model to evaluate its effectiveness in tumor boundary estimation. Fig. 6 presents a comparison of the experimental results obtained from three phantom models (Planar, Curved, Kidney) and an *ex vivo* model. The first column shows the geometry of each model, while the second and third columns display the original stiffness maps and the corresponding outputs reconstructed by SAE, respectively. The original stiffness maps reflect the stiffness contrast between tumor and normal regions but also contain local noise and discontinuities along the boundaries. In contrast, the SAE-reconstructed outputs effectively suppress such noise and enhance the tumor-specific features, yielding smoother and clearer stiffness distributions. This improvement is further emphasized in the clustering results shown in the fourth column of Fig. 6. The predicted tumor boundaries were compared with the ground truth masks defined in Section II-B, and quantitatively evaluated using the metrics in Section II-F. When K-means and GMM were applied directly to the

original stiffness maps, discontinuous clusters and over-segmentation artifacts were observed near the tumor boundaries. By contrast, applying the same algorithms to the SAE-based feature representations produced consistently grouped tumor interiors and more sharply defined boundaries. These findings demonstrate that SAE effectively captures the underlying mechanical characteristics, thereby enhancing clustering stability and improving tumor boundary estimation performance. The entire computation process, including stiffness map generation, feature extraction, and clustering, was completed in an average of 60 seconds per model.

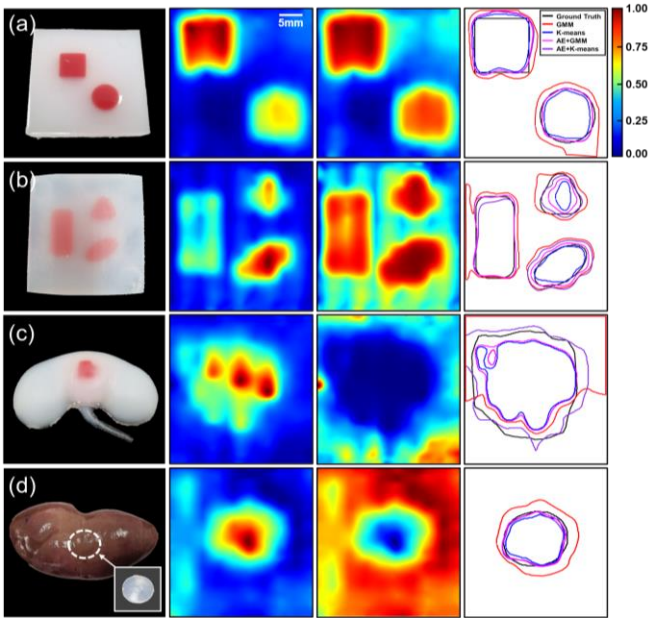


**Fig. 6.** Comparative results across four models. (a) Planar, (b) Curved, (c) Kidney, and (d) *Ex vivo* model. For each model, the first panel illustrates the model structure, the second shows the corresponding original stiffness maps, the third presents the SAE reconstructed outputs, and the fourth depicts the clustering results.

TABLE 1
EVALUATION METRICS ACROSS THE FOUR MODELS

| Model | Method | DSC (%) | Sensitivity (%) | Specificity (%) | HD (mm) | HD95 (mm) | ASSD (mm) |
|---|---|---|---|---|---|---|---|
| Planar | GMM | 80.84 (4.66) | 99.88 (0.02) | 81.99 (7.57) | 5.13 (2.77) | 4.28 (2.54) | 1.98 (0.95) |
| | Kmeans | 91.47 (0.00) | 87.49 (0.00) | 98.59 (0.00) | 2.86 (0.00) | 2.73 (0.00) | 1.60 (0.00) |
| | SAE+GMM | 92.03 (2.37) | 93.81 (6.52) | 96.32 (1.88) | 2.80 (0.13) | 2.60 (0.13) | 1.46 (0.16) |
| | AE+Kmeans | 91.21 (3.24) | 95.77 (4.92) | 94.59 (3.90) | 2.83 (0.16) | 2.62 (0.12) | 1.44 (0.11) |
| Curved | GMM | 70.03 (12.53) | 98.71 (6.19) | 66.70 (17.67) | 4.66 (0.67) | 2.40 (0.35) | 1.14 (0.12) |
| | Kmeans | 60.89 (0.00) | 43.91 (0.00) | 99.89 (0.00) | 3.86 (0.00) | 2.64 (0.00) | 1.93 (0.00) |
| | SAE+GMM | 88.42 (2.84) | 97.91 (1.51) | 91.25 (3.33) | 3.65 (0.17) | 1.31 (0.14) | 0.63 (0.14) |
| | SAE+Kmeans | 86.07 (3.57) | 97.08 (6.92) | 89.47 (4.53) | 3.76 (0.23) | 1.47 (0.33) | 0.74 (0.18) |
| Kidney | GMM | 74.83 (6.87) | 95.04 (0.65) | 61.43 (13.77) | 5.28 (0.99) | 3.36 (0.14) | 1.68 (0.05) |
| | Kmeans | 82.27 (0.00) | 69.94 (0.00) | 99.93 (0.00) | 3.38 (0.00) | 2.18 (0.00) | 1.11 (0.00) |
| | SAE+GMM | 80.16 (2.91) | 67.14 (4.72) | 99.87 (0.28) | 3.56 (0.00) | 2.25 (0.03) | 1.11 (0.05) |
| | SAE+Kmeans | 90.52 (1.32) | 85.11 (2.65) | 97.51 (0.57) | 2.84 (0.03) | 1.95 (0.07) | 0.76 (0.08) |
| *Ex vivo* | GMM | 79.82 (6.19) | 99.99 (0.08) | 91.47 (4.41) | 2.88 (2.28) | 2.49 (1.96) | 1.60 (0.50) |
| | Kmeans | 88.59 (0.00) | 79.81 (0.01) | 99.95 (0.00) | 1.75 (0.00) | 1.43 (0.00) | 0.72 (0.00) |
| | SAE+GMM | 91.39 (6.37) | 88.50 (9.71) | 99.26 (1.59) | 1.37 (0.38) | 1.10 (0.37) | 0.51 (0.31) |
| | SAE+Kmeans | 90.69 (3.92) | 84.61 (0.79) | 99.76 (0.37) | 2.13 (1.04) | 1.64 (1.22) | 0.70 (0.35) |

### *B. Evaluation metrics*

Table 1 summarizes the quantitative evaluation metrics obtained from the tumor boundary estimation experiments performed on the four models, utilizing both region-based metrics (including DSC, sensitivity, and specificity) and distance-based metrics (including HD, HD95, and ASSD). Based on the quantitative results in Table 1, SAE-based clustering outperformed the raw stiffness map–based approach across all models. Both SAE+GMM and SAE+K-means consistently achieved higher DSC values than clustering applied directly to raw stiffness maps, with particularly notable improvements in the curved and kidney models. These findings indicate that SAE effectively extracts discriminative features and enables clearer tumor separation, even in anatomically complex or highly curved structures. Sensitivity was also consistently higher in the SAE-based results, confirming its enhanced ability to detect tumor regions without omission. Meanwhile, specificity remained stable without degradation, demonstrating balanced detection without over-segmentation despite the gains in sensitivity.

The differences were even more pronounced in distance-based metrics such as HD, HD95, and ASSD. In the curved and kidney models, which involve irregular surfaces and multiple tumors, the SAE-based method consistently produced lower HD and HD95 values, as well as significantly reduced ASSD, confirming more precise correspondence between the estimated and ground truth boundaries. These results highlight not only average performance improvements but also the robustness of the SAE-based approach under conditions of higher structural complexity.

Overall, SAE-based feature representations provided statistically significant improvements over the original stiffness map in clustering stability, sensitivity, and boundary accuracy. These quantitative results align with the visual improvements observed in Fig. 6, further supporting the effectiveness of the proposed method for tumor boundary estimation in the models.

Fig. 7 compares the estimated HD values for each model with the predefined threshold. In this study, the threshold was set to approximately 4.5 mm, based on surgical margin requirements reported in the clinical literature, to validate clinical feasibility. Prior studies have recommended maintaining a minimum surgical margin of 1–5 mm in partial nephrectomy and parenchyma-sparing hepatectomy to reduce the risk of recurrence [47], [48], [49], [50]. Accordingly, the HD values, including outliers, were evaluated as the upper safety bound.

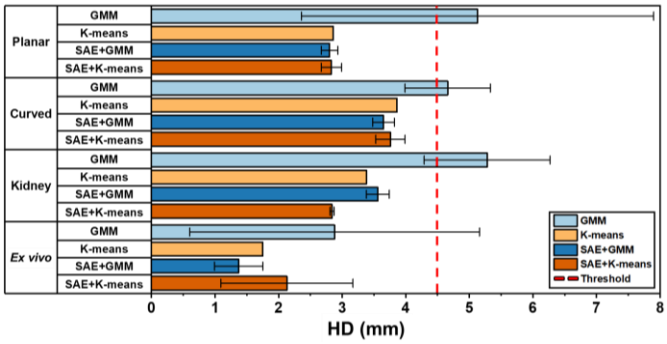


**Fig. 7.** Comparison of tumor boundary estimation results across different models: (a) Planar, (b) Curved, (c) Kidney, and (d) *Ex vivo*.

The results showed that the proposed SAE-based clustering method consistently maintained HD values below the threshold across all models. Notably, even in the kidney model,

which involves higher curvature and anatomical complexity, the HD values did not exceed the threshold. These findings indicate that the proposed method not only enhances boundary detection accuracy but also satisfies clinically required safety margins. Furthermore, this outcome aligns with the improvements in DSC and sensitivity reported in Table 1, providing convergent evidence for both the quantitative enhancement and the clinical potential of the proposed approach.

## IV. Discussion

### *A. Clustering Performance and Clinical Relevance*

In this study, we compared K-means and GMM for tumor boundary estimation and assessed the effect of SAE-based preprocessing. The results showed that, prior to SAE application, the original stiffness maps contained discontinuities and noise that weakened the Gaussian distribution assumption, thereby degrading GMM performance. In contrast, K-means demonstrated relatively stable baseline performance owing to its distance-based partitioning [51]. Following SAE application, noise was effectively suppressed in the low-dimensional latent space, and the structural contrast between tumor and normal regions was enhanced. Consequently, GMM was able to flexibly represent boundary uncertainty using probabilistic mixture distributions, achieving overall improvements in the DSC and sensitivity while maintaining stable specificity. These findings suggest that the SAE+GMM combination provides the most effective approach for maximizing region overlap.

However, in the kidney model, characterized by high curvature and complex boundaries, GMM occasionally overestimated local density, producing fragmented or overlapping clusters instead of clearly defined tumor–normal boundaries. This resulted in reduced boundary sharpness. In such anatomically complex scenarios, SAE+K-means may provide a more robust alternative by mitigating the tendency of GMM toward over-segmentation.

In addition, the proposed method consistently maintained HD values below the clinically defined threshold of 4.5 mm across all phantom and *ex vivo* models, while ASSD was also significantly reduced. Because boundary precision is directly associated with securing safe surgical margins, these findings underscore the clinical relevance of the approach. Notably, high accuracy was achieved using stiffness data derived solely from a single F/T sensor, highlighting strong potential for surgical translation. Compared with previously reported ultrasound-based segmentation studies, which reported $HD95 = 8.90 \pm 0.15$ mm and $ASSD = 2.87 \pm 0.05$ mm [52], the proposed method achieved $HD95 \leq 2.6$ mm and $ASSD \leq 1.1$ mm, reflecting a two- to threefold improvement in boundary precision. Collectively, these results suggest that the proposed approach offers a more practical and competitive performance than conventional image-based methods for intraoperative tumor boundary estimation.

### *B. Considerations for Clinical Translation*

This study estimates tumor boundaries by constructing a 2D stiffness map from sweeping palpation data. In RMIS proce dures where resection proceeds along the normal direction, such 2D boundary information is often sufficient for determin ing an appropriate surgical margin [53]. However, the three dimensional geometry and depth of the tumor remain critical for surgical precision. Because soft tissues exhibit nonlinear force-displacement behavior that varies with indentation depth, a 2D stiffness map obtained at a fixed palpation depth provides only a surface projection of the underlying mechanical distribution and cannot fully characterize deeper lesions. To address this limitation, future work will incorporate multi-depth stiffness measurements, subsurface geometric cues, and learning-based mechanical models to estimate full 3D stiffness distributions.

In addition, the *ex vivo* experimental setup does not account for physiological disturbances such as respiration, organ in teraction, or tissue deformation during palpation, which can degrade stiffness estimation accuracy. To mitigate this, we plan to develop a dynamic compensation framework that leverages F/T sensor torque data for real-time disturbance detection and adaptive control.

Moreover, the initial surface scanning step, currently per formed through manual teleoperation under impedance control, will be upgraded to an automated hybrid-control scanning sys tem to improve consistency and reproducibility during surface reconstruction.

Finally, the current palpation tool prototype has exposed electrical components, limiting its clinical applicability. A re designed, fully sealed, and autoclavable housing will be devel oped to meet surgical hygiene and safety requirements.

## V. Conclusion

In this study, we proposed a tumor boundary detection method for RMIS that integrates SAE-based feature learning with unsupervised clustering of sweeping palpation data acquired from a single F/T sensor. This approach effectively suppressed noise and enhanced tumor-related features, thereby enhancing clustering stability, clarifying boundaries, and achieving high consistency with the ground truth across both phantom models and an *ex vivo* model. Notably, significant improvements were observed in DSC and sensitivity, accompanied by reductions in HD and ASSD. Even in the anatomically complex kidney model, the proposed method satisfied the clinically relevant threshold while delivering a two- to threefold improvement in precision compared with conventional image-based methods. These results highlight the clinical potential of the proposed approach for minimizing surgical margins and preserving organ function in RMIS. Looking ahead, future work will aim to further improve tumor boundary estimation by incorporating semi-supervised learning and deep clustering strategies into the robotic palpation framework.

## REFERENCES


[1] B. S. Peters et al., "Review of emerging surgical robotic technology," Surg. Endoscopy, vol. 32, no. 4, pp. 1636–1655, Apr. 2018.

[2] V. Vitiello et al., "Emerging robotic platforms for minimally invasive surgery," IEEE Rev. Biomed. Eng., vol. 6, pp. 111–126, 2013.

[3] U. Kim et al., "A surgical palpation probe with 6-axis force/torque sensing capability for minimally invasive surgery," IEEE Trans. Ind. Electron., vol. 65, no. 3, pp. 2755–2765, Mar. 2018.

[4] P. Kumar et al., "Surgeon perception of factors affecting the efficiency of conventional and robotic laparoscopy: A Pan India study," Heliyon, vol. 8, no. 12, 2022.

[5] D. Fasanella et al., "Intraoperative imaging techniques for robotic-assisted partial nephrectomy," Front. Surg., vol. 11, 2024.

[6] X. Zeng et al., "Efficacy of laparoscopic parenchyma-sparing hepatectomy with ARN-FI guidance for CRLMs," Int. J. Surg., vol. 117, pp. 10001–10002, 2025.

[7] A. Yurtbay et al., "The impact of surgical margin distance on local recurrence and survival in patients with soft tissue sarcoma," Medicina, vol. 61, no. 2, 2025, Art. no. 289.

[8] Y. Lin et al., "Prognostic impact of surgical margin in hepatectomy on patients with hepatocellular carcinoma: A meta-analysis of observational studies," Front. Surg., vol. 9, no. 810479, pp. 1–13, 2022.

[9] N. Marahrens et al., "An ultrasound-guided system for autonomous marking of tumor boundaries during robot-assisted surgery," IEEE Trans. Med. Robot. Bionics, vol. 6, no. 4, pp. 1699–1712, Nov. 2024.

[10] G. Santini et al., "Kidney tumor segmentation using an ensembling multi-stage deep learning approach. A contribution to the KiTS19 challenge," 2019, arXiv:1909.00735.

[11] S. Gul et al., "Deep learning techniques for liver and liver tumor segmentation: A review," Comput. Biol. Med., vol. 147, 2022, Art. no. 105620.

[12] H. Liu et al., "Rolling indentation probe for tissue abnormality identification during minimally invasive surgery," IEEE Trans. Robot., vol. 27, no. 3, pp. 450–460, Jun. 2011.

[13] P. A. Wise et al., "Intraoperative liver deformation and organ motion caused by ventilation, laparotomy, and pneumoperitoneum in a porcine model for image-guided liver surgery," Surg. Endosc., vol. 38, pp. 1379–1389, 2024.

[14] F. Alam, "Medical image registration in image guided surgery: Issues, challenges, and opportunities," Comput. Methods Programs Biomed., vol. 163, pp. 15–35, 2018.

[15] N. Zevallos et al., "A surgical system for automatic registration, stiffness mapping and dynamic image overlay," in Proc. IEEE/RSJ Int. Conf. Intell. Robots Syst, 2017, pp. 5370–5375.

[16] C. Hou et al., "A highly integrated 3D MEMS force sensing module with variable sensitivity for robotic-assisted minimally invasive surgery," Adv. Funct. Mater., vol. 33, no. 43, pp. 1–13, Oct. 2023.

[17] A. Samani, M. Bishop, C. Luginbuhl, and D. Plewes, "Techniques for characterizing mechanical properties of soft tissues," Phys. Med. Biol., vol. 48, no. 22, pp. R1–R23, 2003.

[18] J. Liu, W. Tan, and J. Chen, "Matrix stiffness-driven cancer progression and the targeted therapeutic strategy," J. Hematol. Oncol., vol. 15, no. 1, 2022, Art. no. 103.

[19] C. Huang et al., "Tactile Perception Technologies and their applications in minimally invasive surgery: A review," Front. Physiol., vol. 11, 2020, Art. no. 611596.

[20] E. Samur et al., "A robotic indenter for minimally invasive measurement and characterization of soft tissue response," Med. Image Anal., vol. 11, no. 4, pp. 361–373, Aug. 2007.

[21] M. Beccani et al., "Wireless tissue palpation for intraoperative detection of lumps in the soft tissue," IEEE Trans. Biomed. Eng., vol. 61, no. 2, pp. 353–361, Feb. 2014.

[22] T. Li et al., "A high-sensitivity tactile sensor array based on Fiber bragg grating sensing for tissue palpation in minimally invasive surgery," IEEE/ASME Trans. Mechatron., vol. 23, no. 5, pp. 2306–2315, Oct. 2018.

[23] K. A. Nichols and A. M. Okamura, "Autonomous robotic palpation: Machine learning techniques to identify hard inclusions in soft tissues," in ∗Proc. IEEE Int. Conf. Robot. Autom.∗, Karlsruhe, Germany, 2013, pp. 4384–4389.

[24] M. Mir et al., "A minimally invasive robotic tissue palpation device," IEEE Trans. Biomed. Eng., vol. 71, no. 6, pp. 1958–1968, Jun. 2024.

[25] J. Wang et al., "Image-to-force estimation for soft tissue interac-tion in robotic-assisted surgery using structured light," Jan. 2025, arXiv:2501.08593.

[26] M. Hwang et al., "Applying depth-sensing to automated surgical manipulation with a da Vinci robot," in Proc. Int. Symp. Med. Robot., 2020.

[27] O. Bin-Alamer et al., "Intraoperative imaging and optical visualization techniques for brain tumor resection: A narrative review," Cancers, vol. 15, no. 19, Oct. 2023, Art. no. 4890.

[28] Y. Zhang et al., "Action augmentation of tactile perception for soft-body palpation," IEEE Robot. Autom. Lett., vol. 6, no. 4, pp. 7113–7120, Oct. 2021.

[29] N. Bandari, J. Dargahi, and M. Packirisamy, "Tactile Sensors for minimally invasive surgery: A review of the State-of-the-art, applications, and perspectives," IEEE Access, vol. 8, pp. 7682–7708, 2020.

[30] R. Uppuluri, A. Bhattacharjee, S. Anwar, and Y. She, "SeeBelow: Subdermal 3D reconstruction of tumors with surgical robotic palpation and tactile exploration," in Proc. IEEE/RSJ Int. Conf. Intell. Robots Syst., Abu Dhabi, UAE, 2024, pp. 6961–6968.

[31] S. McKinley et al., "A single-use haptic palpation probe for locating subcutaneous blood vessels in robot-assisted minimally invasive surgery," in Proc. IEEE Int. Conf. Automat. Sci. Eng., Gothenburg, Sweden, 2015, p. 1151–1158.

[32] J. Francis et al., "A cable driven robotic palpation system for prostate palpation," Int. J. Med. Robot. Comput. Assist. Surg., vol. 18, no. 6, Dec. 2022, Art. no. e2435.

[33] Y. Guo et al., "Compensating uncertainties in force sensing for robotic palpation," Appl. Sci., vol. 9, no. 12, 2019, Art. no. 2573.

[34] C. Stashko et al., "A convolutional neural network STIFMap reveals associations between stromal stiffness and EMT in breast cancer," Nature Commun., vol. 14, 2023, Art. no. 3561.

[35] A. H. Akash et al., "SW ViT: A Spatio Temporal vision transformer network with Post Denoiser for Sequential Multi push ultrasound shear wave elastography," 2025, arXiv:2505.18865.

[36] J. Hong et al., "Intraoperative tumor localization using sweeping palpation in robot-assisted minimally invasive surgery (RMIS)," IEEE Robot. Autom. Lett., vol. 10, no. 9, pp. 8898–8905, Sep. 2025.

[37] R. C. O. Locke and R. V. Patel, "Optimal remote center-of-motion location for robotics-assisted minimally-invasive surgery," in Proc. IEEE Int. Conf. Robot. Autom., Rome, Italy, 2007, pp. 1900–1905.

[38] N. Hogan, "Impedance control: An approach to manipulation," in Proc. Amer. Control Conf., San Diego, CA, USA, 1984, pp. 304–313.

[39] S. W. Bang et al., "Registration-free minimally invasive surgery without preoperative phase," Int. J. Control Autom. Syst., vol. 21, pp. 3313–3323, 2023.

[40] R. Hanocka et al., "Point2Mesh: A self-prior for deformable meshes," ACM Trans. Graph., vol. 39, no. 4, Jul. 2020, Art. no. 126.

[41] A. Masood et al., "Tool path generation for complex surface machining using point cloud data," in Proc. 12th Glob. Conf. Sustain. Manuf., vol. 26, 2015, pp. 397–402.

[42] T. M. Cover and P. E. Hart, "Nearest neighbor pattern classification," IEEE Trans. Inf. Theory, vol. 13, no. 1, pp. 21–27, Jan. 1967.

[43] R. Huben et al., "Sparse autoencoders find highly interpretable features in language models," in Proc. Int. Conf. Learn. Represent., 2024.

[44] S. Kullback and R. A. Leibler, "On information and sufficiency," Ann. Math. Statist., vol. 22, no. 1, pp. 79–86, 1951.

[45] J. H. Wolfe, "Pattern clustering by multivariate mixture analysis," Multivariate Behav. Res., vol. 5, no. 3, pp. 329–350, 1970.

[46] J. A. Hartigan and M. A. Wong, "Algorithm AS 136: A k-means clustering Algorithm," J. R. Statist. Soc. C (Appl. Statist.), vol. 28, no. 1, pp. 100–108, 1979.

[47] P. Bilic et al., "The liver tumor segmentation benchmark (LiTS)," Med. Image Anal., vol. 84, 2023, Art. no. 102680.

[48] M. M. E. L. Henderickx et al., "Surgical margins after partial nephrectomy as prognostic factor for the risk of local recurrence in pT1 RCC: A system-atic review and narrative synthesis," World J. Urol., vol. 40, pp. 1833–1845, 2022.

[49] J. Lee et al., "Evaluation of the surgical margin threshold for avoiding recurrence after partial nephrectomy in patients with renal cell carcinoma," Yonsei Med. J., vol. 63, no. 2, pp. 173–178, 2022.

[50] K. Sakamoto et al., "Prognostic impact of surgical margin width in hepatectomy for colorectal liver metastasis," Cancers, vol. 15, no. 5, 2023, Art. no. 1450.

[51] V. Roizman et al., "A flexible EM-like clustering algorithm for noisy data," IEEE Trans. Pattern Anal. Mach. Intell., vol. 46, no. 5, pp. 2707–2721, 2023.

[52] Z. Tang et al., "MLAU-Net: Deep supervised attention and hybrid loss strategies for enhanced segmentation of low-resolution kidney ultrasound," Comput. Biol. Med., vol. 181, 2024, Art. no. 109442.

[53] S. C. Campbell et al., "Guideline for management of the clinical T1 renal mass," J. Urol., vol. 182, no. 4, pp. 1271–1279, 2009.